Progress In Electromagnetics Research, Vol. 128, 171–193, 2012

NOVEL PRE-PROCESSING TECHNIQUES FOR COHERENCE IMPROVING IN ALONG-TRACK DUAL-CHANNEL LOW FREQUENCY SAR

C.-Y. Fan*, X.-T. Huang, T. Jin, J.-G. Yang, and D.-X. An

School of Electronic Science and Engineering, National University of Defense Technology, Changsha, Hunan 410073, China

Abstract—The coherence between the complex image pair from two channels is important for improving the capability of along-track interferometry (ATI) processing in synthetic aperture radar (SAR) ground moving target indication (GMTI). The along-track dual-channel low frequency SAR can be easily influenced by not only mismatch errors of the image pair but also the radio frequency interference (RFI). RFI has great impacts on the joint probability density function (PDF) of magnitude and phase in the interferometric image. However, little work has been done to investigate the coherence improvement under RFI. This study develops an algorithm to improve the coherence of the image pair for along-track dual-channel low frequency SAR, which can be used by ATI. After analyzing RFI imaging in detail, it is proposed that the along-track interferometric image in the range frequency and cross-range slow time domain can be used to detect RFI. Median filters are proposed to further suppress RFI. This suppression has the same implementations to the image pair without heavy computation load. Considering RFI suppression and mismatch errors compensation, a pre-processing flow is proposed to achieve high coherence of the interferometric image in low frequency SAR. It is shown that the coherence of the complex image pair can be improved greatly by using this pre-processing flow. The effectiveness of this algorithm is demonstrated with real data acquired by an airborne along-track dual-channel P-band SAR GMTI system.

1. INTRODUCTION

Along-track interferometry (ATI) is an operational and easy way in ground moving target indication (GMTI) with along-track dual-

Received 15 January 2012, Accepted 15 May 2012, Scheduled 27 May 2012

* Corresponding author: Chongyi Fan (fancoeeoc@yahoo.com.cn).

channel synthetic aperture radar (SAR) [1–4], but the interferometric phase is very sensitive to the coherence of the complex image pair. In high frequency SAR system, thermal noise in the channels, imbalanced receiver hardware or different antenna gain patterns may add interference to the returned echo. The differences of channel transfer functions or antenna beam patterns can result in the systematic phase errors in the interferogram [5–9]. All of them will degrade the coherence of the image pair and distort the moving target detection using ATI. To guarantee the performance of ground moving target indication (GMTI), the coherence of the complex image pair should be high enough.

Low frequency SAR [10–13] can detect moving targets concealed in forest or under camouflage. However, this system has not only mismatch errors similar to that in high frequency system but also the radio-frequency interference (RFI). The coherence will be degraded by both of them. Radio-frequency bands are occupied by communication systems, such as television, FM radio, narrowband FM (NBFM) two-way radio repeaters, and other sources [14, 15]. These narrow bandwidth interferences, changing from one pulse to another, will degrade image quality and bring interferometric phase errors [16–18]. Up to now, RFI suppression methods of SAR mainly focused on improving image quality with raw data collected by a single channel. The methods based on unknown range frequency, such as adaptive filtering [14, 19, 20] and channel equalization [21], do not need to estimate the parameters of interference signal. They are more practical than the methods based on known range frequency. However, adaptive filtering with complicated implementation may leave interferences unsuppressed in the fluctuating clutter. The filtering is implemented on each channel respectively. The differences of implementations will introduce extra mismatch errors to degrade the coherence of the image pair. Channel equalization is easier and more effective in real-time imaging, but this suppression method will easily leave unsuppressed RFIs which have narrow bandwidths and weak energies. It's noted that the influence of RFI to the interferometric phase is much stronger than that to the magnitude [15–18]. Therefore the suppression methods aiming at improving image quality are insufficient to the along-track interferometric image.

Few literatures have considered RFI suppression for the interferometric image, except the algorithm based on coherent estimation with subtraction of interfering signals adaptive filtering [22] and notch-filtering of the interferences with focused SAR images [18]. These suppression methods belong to the adaptive filtering methods, which are implemented in each channel respectively. Both of them

assume that RFI can be suppressed complete and there is no phase differences left from receiving channels or suppression procedure. Actually, the unsuppressed RFI is unavoidable in real data processing. It has little influence on the magnitude image, but it may destroy the joint probability density function (PDF) of magnitude and phase in the interferometric image as explained in Section 2. The conventional pre-processing of ATI aimed at improving the coherence, only contains the channel balancing techniques and accurate image coregistration methods [5–9, 23, 24]. Therefore, it cannot satisfy the applications of ATI in the low frequency SAR system with unsuppressed RFI. When the load of platform is light, like unmanned aerial vehicle (UAV) [25, 26], it is also necessary to use a simple pre-processing flowchart for the real-time processing.

In this paper, novel pre-processing techniques consisting of two parts are developed to improve the coherence of along-track dual-channel low frequency SAR. In the first part, the characteristics of RFI in the focused image are analyzed and a novel suppression approach considering phase errors from weak RFI is proposed for along-track interferometric image. In the second part, mismatch errors in dual-channel low frequency SAR are analyzed with the corresponding compensation in different data domains. The proposed algorithm is an attractive approach for several reasons: (a) The interferences can be suppressed almost completely for the applications by interferometric phase; (b) No extra error will be brought from the differences of implementations in each channel; (c) some possible error sources that degrade the coherence of dual-channel low frequency SAR are included; and (d) both the suppression and error compensation only use non-adaptive filtering, such as the median filter, which can reduce the computation complexity and facilitate real-time implementation.

The basic principle of coherence improving algorithm proposed here is very similar to that in [9], where a 2-dimension (2-D) phase error reduction technique was proposed to maximize the coherence of image pair for moving vehicle detection. However, our paper considers the distortion to the interferometric image caused by unsuppressed RFI and various errors for the low frequency system. Both the RFI suppression and error correction can be united in the pre-processing flow based on the real-time SAR images, which are obtained from the data acquired pulse by pulse.

This paper is organized as follows. In Section 2, the properties of RFI on the interferometric image and the focused image in the range frequency and cross-range slow time domain are analyzed in detail. In Section 3, a novel suppression approach is proposed for the along-tack interferometric image. In Section 4, various errors in low frequency

system are considered and an algorithm for improving the coherence is presented. In Section 5, the performance is analyzed and verified by both simulation and experimental results. The real along track low frequency SAR data is acquired by an airborne along-track dual-channel P-band SAR GMTI system. Section 6 concludes the paper. In the following context, we use the frequency-time domain for the range frequency and cross-range slow time domain, the time domain for the range fast time and cross-range slow time (2-D time) domain, and the frequency domain for the range frequency and cross-range frequency (2-D frequency) domain for simplicity.

2. PROPERTIES OF RFI

It is noted that during the real-time processing, it is easy to meet the case that unsuppressed RFI are left in the interferometric image in the low frequency SAR system. The statistical results based on the real data will show that these unsuppressed RFI will distort the joint PDF of interferometric magnitude and phase. Figure 1(a) describes the joint PDF from a small region of the airborne along track low frequency SAR scene. This scene is the same as the following one that Figure 2(a) describes in this section. The region is the area-A as marked in the Figure 5 in Section 5. Since there are no interferences, the interferometric phases of most pixels are close to zero and the distribution is identical with the theoretical one in [1, 27]. Figure 1(b) describes the joint PDF of the same region under RFI. The magnitude distribution remains nearly the same, so under this interference the magnitude image still has good quality. The SAR image in the Figure 2(a) verifies it.

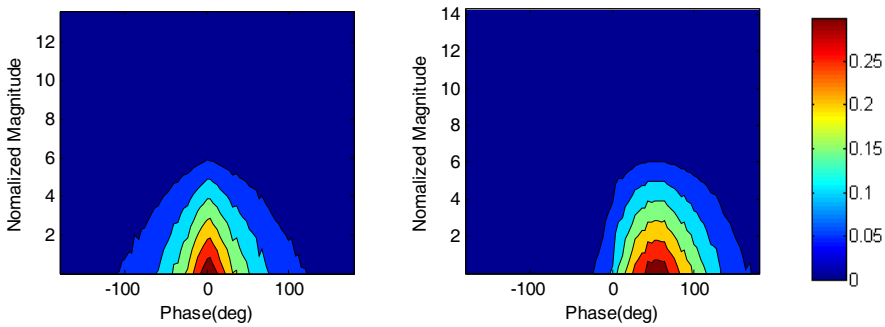

Figure 1. The joint PDF of interferometric magnitude and phase. (a) Using scene without RFI. (b) Using scene with RFI.

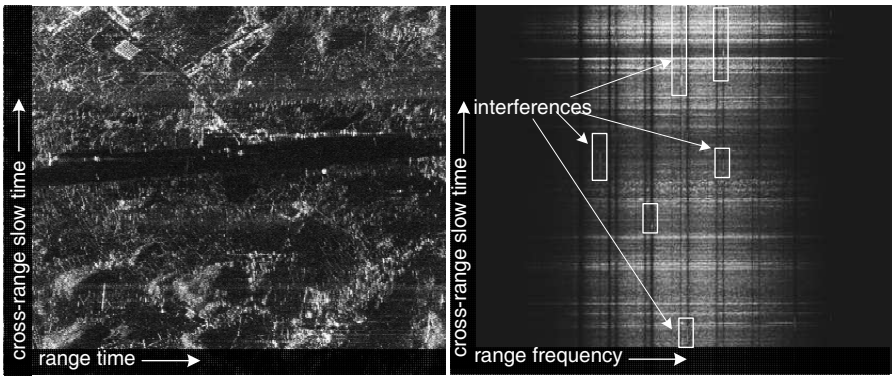

(a) (b)

Figure 2. (a) The magnitude image of an airborne P-band SAR scene with unsuppressed interferences. The magnitude image appears not deteriorated by interferences after channel equalization. (b) The frequency-time domain of the scene image. Some of interferences have been marked.

However, the phases of most pixels in Figure 1(b) are far away from zero, whose values are around a fixed phase. The reason lies in the fact that when the RFI is larger than the clutter, the formed complex-valued image pixel is dominated by the RFI. Since the RFI is directionally sensitive, the RFI received by the two channels are different. Therefore, the interferometric phases of the image formed by received echo of the two channels are not zero in the area dominated by the RFI, which reduces the coherence of the image pair eventually.

Conventionally, in the real-time processing, RFI suppression is operated on the range frequency azimuth time (frequency-time) domain of raw data. The interference is focused in this domain. This is beneficial for suppression by its high energy. But the suppression in this domain must preserve the phase for the following azimuth compression, which cannot consider phase suppression. Once there is interference left, the distortion to the joint PDF is unavoidable. Moreover, if the suppression is implemented in each channel respectively, there will be an extra error in the interferometric image from the differences of implementations. The following context and simulation will show that the image in the frequency-time domain is also suitable for RFI suppression, especially for the interferometric phase.

Suppose the received RFI signals are a sum of complex sinusoid signals [14]. In the ith channel ($i = 1, 2$), a single RFI signal at range

frequency f_l can be written as

$$ss_l^i(\tau, t_m) = \left[\rho_l \text{rect}\left(\frac{t_m - t_l^i}{T_l}\right) \exp\left(j\varphi_l^i(t_m)\right)\right] \cdot \exp(j2\pi f_l \tau) \quad (1)$$

where τ and t_m denote the range fast time and cross-range slow time, respectively. The term in the square bracket indicates the part that RFI signal varies with the slow time t_m, where ρ_l denotes the magnitude, rect $\left(\frac{t_m - t_l^i}{T_l}\right)$ denotes the azimuth rectangular window of the i channel with the center time t_l^i and the duration T_l. The phase of RFI $\varphi_l^i(t_m)$ will change from one pulse to another. Equation (1) uses the following hypotheses: (a) Both the magnitude ρ_l and the range frequency f_l are invariable during T_l; (b) The RFI has a narrow bandwidth, which can be distinguished in the frequency-time domain; (c) The phase $\varphi_l^i(t_m)$ changes with t_m slowly, which can be assumed as a wide sense stationary (WSS) process with the mean value of phase $\bar{\varphi}_l^i$; (d) And there exists the expectation of phase difference $\Delta\varphi_l = \bar{\varphi}_l^1 - \bar{\varphi}_l^2$. Under the assumption of WSS, the expression of RFI in the 2-D frequency domain can be expressed as:

$$\mathbb{FT}\left\{ss_l^i(\tau, t_m)\right\} = \rho_l \exp\left(j\bar{\varphi}_l^i\right) \frac{\sin(\pi f_a T_l)}{\pi f_a} \delta(f_l - f_r) \exp\left(-j2\pi f_a t_l^i\right) \quad (2)$$

where $\mathbb{FT}$ denotes 2-D Fourier transformation, and f_r and f_a denote the range and azimuth frequency, respectively. The impulse response $\delta(\cdot)$ ignores the scaling of magnitude from the azimuth rectangular window.

Assume that the radar platform moves at a constant velocity v_a along a straight path and transmits linear frequency modulation pulses at the center frequency f_c. The 2-D compensation function for imaging a static target at slant range R_0 can be expressed as [28]:

$$H(f_r, f_a) = \exp\left(j\frac{4\pi R_0(f_r + f_c)}{c}\sqrt{1 - \frac{c^2 f_a^2}{4v_a^2(f_r + f_c)^2}} + j\frac{\pi f_r^2}{K_r}\right) \quad (3)$$

where K_r is the range modulation slope and c the speed of light. Equation (3) can be divided into two parts: the range compression function

$$H_r(f_r) = \exp\left(j\frac{\pi f_r^2}{K_r}\right) \quad (4)$$

and the azimuth compression function including the coupling term between range and azimuth:

$$H_a(f_r, f_a) = \exp\left(j\frac{4\pi R_0(f_c + f_r)}{c}\sqrt{1 - \frac{c^2 f_a^2}{4v_a^2(f_c + f_r)^2}}\right) \quad (5)$$

Therefore, the expression of RFI in the frequency domain after SAR imaging can be written as:

$$\mathbb{FT}\left\{ss_l^i(\tau,t_m)\right\}\cdot H(f_r,f_a)=\mathbb{FT}\left\{ss_l^i(\tau,t_m)\right\}\cdot H_r(f_r)\cdot H_a(f_r,f_a)$$
$$=\rho_l\exp\left(j\bar{\varphi}_l^i\right)\exp\left(j\frac{\pi f_l^2}{K_r}\right)\delta(f_l-f_r)F(f_a) \quad (6)$$

where

$$F(f_a) = \frac{\sin(\pi f_a T_l)}{\pi f_a}\exp\left(j\frac{4\pi R_0(f_c+f_l)}{c}\sqrt{1-\frac{c^2f_a^2}{4v_a^2(f_c+f_l)^2}}\right)$$
$$\exp\left(-j2\pi f_a t_l^i\right) \quad (7)$$

Therefore, the expression of RFI in the frequency-time domain can be calculated as follows:

$$Ss_l^i(f_r,t_m) = \int\mathbb{FT}\left\{ss_l^i(\tau,t_m)\right\}\cdot H(f_r,f_a)\cdot\exp(j2\pi t_m f_a)\,\mathrm{d}f_a$$
$$= \rho_l\exp\left(j\bar{\varphi}_l^i\right)\exp\left(j\frac{\pi f_l^2}{K_r}\right)\delta(f_l-f_r)\,f\left(t_m-t_l^i\right) \quad (8)$$

According to the principle of stationary phase (POSP) [28], $f\left(t_m-t_l^i\right)$ can be deduced as a line along the cross-range slow time. It will be easy to understand this characteristic of RFI distribution when we use the approximate azimuth compensation function $\tilde{H}_a(f_a)=\exp\left(-j\frac{\pi f_a^2}{K_a}\right)$, where K_a is the azimuth modulation slope. By this approximate function, the analytical expression of $f\left(t_m-t_l^i\right)$ can be written as:

$$\tilde{f}\left(t_m-t_l^i\right)=T_l\,\mathrm{sin\,c}\left(\pi K_a T_l\left(t_m-t_l^i\right)\right)\exp\left(j\pi K_a\left(t_m-t_l^i\right)^2\right) \quad (9)$$

It can be noted from (9) that the duration of RFI in the slow time increases to the range of t_m, as well as the duration of azimuth compression function — the synthetic aperture time T_a. Therefore, the RFI signal in the frequency-time domain is distributed as a line. Usually, the duration T_l of RFI is short and the 3 dB width of the main lobe of sinc function is large. So the magnitude of RFI varies slowly under the system parameters of real scene and lasts a longer time than T_l. Here we denotes this longer time as T_l'. Substituting the expression (9) into (8), the RFI signal in frequency-time domain can be simplified as:

$$Ss_l^i(f_r,t_m)=A_{l,m}^i\exp\left(j\bar{\varphi}_l^i\right)\delta(f_l-f_r) \quad (10)$$

where

$$A_{l,m}^i=\rho_l\,\mathrm{sin\,c}\left(\pi K_a T_l\left(t_m-t_l^i\right)\right)\exp\left(j\frac{\pi f_l^2}{K_r}\right)\exp\left(j\pi K_a\left(t_m-t_l^i\right)^2\right) \quad (11)$$

and ρ_l is the magnitude of RFI in this domain. After the image registration, the difference time of t_l^i can be compensated, i.e., $A_{l,m} = A_{l,m}^i$. As a result, the main difference of RFI signal is the interferometric phase $\Delta\varphi_l$ in the interferometric image of the frequency-time domain.

However, the RFI signal has a narrow bandwidth in practice, which brings a coupling term between range and cross-range. With the imaging parameters of the static target and some approximations to $H_a(f_a, f_r)$, there may be a curve to the distribution of RFI in the frequency-time domain image. Fortunately, the curvature of the curve is so small that it will not influence the application of our approach, especially when the low frequency SAR uses high precise imaging algorithms, like non-linear chirp scaling algorithm (NCSA) and omega-k algorithm [28–30]. Figure 2(b) illustrates an example of an airborne low frequency SAR data which is transformed into the frequency-time domain. The interferences are visible as long lines with little curvature, which have been marked in the rectangles. These interferences are very weak, so that the quality of the image magnitude is not deteriorated by them, as shown in Figure 2(a).

3. THE SUPPRESSION ALGORITHM

Based on the properties of RFI, the characteristics of the interferometric image in the frequency-time domain are considered first. Suppose there are L RFI signals in a $N \times M$ (range $\times$ cross-range) image. The frequency-time domain of these interferences can be expressed as:

$$S_i(f_r, t_m) = \sum_{l=1}^{L} Ss_l^i(f_r, t_m) = \sum_{l=1}^{L} A_{l,m} \exp\left(j\bar{\varphi}_l^i\right) \delta(f_l - f_r) \tag{12}$$

The subscript m denotes the slow time t_m, $m = 1, 2, \ldots, M$. The frequency-time domain image of the ith channel can be expressed as:

$$X_i(f_r, t_m) = Z_i(f_r, t_m) + S_i(f_r, t_m) \tag{13}$$

$Z_i(f_r, t_m)$ is a coherent sum of scene clutters, moving target and image noise. In the frequency-time domain, it is distributed along the range frequency at the slow time t_m and is orthogonal to the distribution line of RFI. So the frequency-time domain interferometric image can be expressed as:

$$I(f_r, t_m) = X_1(f_r, t_m) \cdot X_2^*(f_r, t_m) = \rho_x^2(f_r, t_m) \exp\left(j\Delta\vartheta(f_r, t_m)\right) \tag{14}$$

with the magnitude $\rho_x^2(f_r, t_m)$ and the phase $\Delta\vartheta_m(f_r)$ of the interferometric image $I(f_r, t_m)$. $\rho_x(f_r, t_m)$ can be considered as the magnitude of pixel in the image $X_i(f_r, t_m)$.

When the pixel of $I(f_r, t_m)$ does not contain the RFI signal, Equation (14) can be expressed as:

$$I(f_r, t_m) = Z_1(f_r, t_m) \cdot Z_2^*(f_r, t_m) \tag{15}$$

In this case, the interferometric phase indicates the motion of target. Since the moving target is usually covered by static clutter in frequency-time domain, there is $\Delta\vartheta(f_r, t_m) \approx 0^\circ$. When the pixel of $I(f_r, t_m)$ contains the RFI, the interferometric phase $\Delta\vartheta(f_r, t_m)$ may be far away from zero. Assuming $Z_i(f_r, t_m)$ follows the complex Gaussian distribution $CN\left(0, \sigma_0^2/N\right)$, with the variation σ_0 of the time domain image. The expectation of Equation (14) at the range frequency f_l can be written as:

$$\overline{I(f_r, t_m)} \approx \frac{1}{N}\sigma_0^2 + \rho_l^2 \exp(j\Delta\varphi_l)\,\delta(f_l - f_r) \tag{16}$$

The expression (16) is a biased estimation of the RFI signal, as well as the maximum likelihood estimation [31] of RFI at the frequency f_l. The extra interferometric phase $\Delta\varphi_l$ will help us detect RFI.

Based on the above analyses, the novel suppression approach for along-track dual-channel low frequency SAR is proposed as follows:

Step 1, detection of RFI signal in the interferometric image of the frequency-time domain.

In this step a binary mutually exclusive hypothesis detector is proposed to detect whether the pixel of $I(f_r, t_m)$ is influenced by RFI as $\mathbf{H}_1$ or not as $\mathbf{H}_0$:

$$\begin{cases} \mathbf{H}_0: & \rho_x^2(f_r, t_m) < (\gamma_0\bar{\rho}_m)^2 \text{ or } \left|\Delta\vartheta(f_r, t_m) - \Delta\bar{\vartheta}_m\right| < 0 \\ \mathbf{H}_1: & \rho_x^2(f_r, t_m) \geq (\gamma_0\bar{\rho}_m)^2 \text{ and } \left|\Delta\vartheta(f_r, t_m) - \Delta\bar{\vartheta}_m\right| \geq 0 \end{cases} \tag{17}$$

where $|\cdot|$ denotes the absolute sign and $(\gamma_0\bar{\rho}_m)^2$ the threshold of interferometric magnitude. Here $\bar{\rho}_m$ is the expectance of $\rho_x(f_r, t_m)$ at the slow time t_m and γ_0 the weighting constant. $\Delta\bar{\vartheta}_m$ is the expectation of absolute value of $\Delta\vartheta(f_r, t_m)$, and it denotes the threshold of interferometric phase. This detector can estimate the duration T_l' of RFI signal in frequency-time domain by the detection of pixels. It is similar to the detector of ATI in the time domain image, except that both interferometric magnitude and phase thresholds can change with the slow time. It can apply to the complicated scenes in practice. Moreover, the simulation results in [32] indicate that $\gamma_0 = 0.5$ and $\Delta\bar{\vartheta}_m = 15^\circ$ are suitable for this detector, when the moving target is flooded by static clutter.

Step 2, suppression of the magnitude.

Based on the above detection, the median filtering is implemented in the frequency-time image of each channel to suppress the magnitude of RFI and to revert the magnitude of scene clutter $\tilde{X}_i(f_r, t_m)$ from $X_i(f_r, t_m)$:

$$\begin{cases} \tilde{X}_i(f_r, t_m) = \text{MedFilter}\left[|X_i(f_r, t_m)|\right] \cdot \exp\left(j\angle X_i(f_r, t_m)\right) \\ \qquad\qquad\qquad\qquad\qquad\qquad \text{if } f_r = f_l, t_m \in T_l' \\ \tilde{X}_i(f_r, t_m) = X_i(f_r, t_m) \qquad\qquad \text{if } f_r \neq f_l,\ t_m \notin T_l' \end{cases} \tag{18}$$

where $\angle\cdot$ denotes the phase angle and MedFilter $[\cdot]$ the median filtering. The bandwidth of median filter is twice more than the one of detected RFI.

Step 3, suppression of the interferometric phase.

In this step, another median filter is implemented in the frequency-time interferometric image to suppress the interferometric phase of RFI and to estimate the interferometric phase without RFI, which can be expressed as:

$$\hat{X}_2(f_r, t_m) = \tilde{X}_2(f_r, t_m) \cdot \exp\left(j \cdot \text{MedFilter}\left[\Delta\vartheta_m(f_r)\right] - j \cdot \Delta\vartheta_m(f_r)\right) \quad \text{if } f_r = f_l, t_m \in T_l' \tag{19}$$

The bandwidth of this median filter is twice more than that of interferometric phase from the detected RFI. Equation (19) is only implemented on $\tilde{X}_2(f_r, t_m)$, which is influenced by RFI. The other part of $\hat{X}_i(f_r, t_m)$ is the same as $\tilde{X}_1(f_r, t_m)$. This step will preserve the interferometric phase of possible moving target in the scene. The inverse Fourier transforms of $\hat{X}_i(f_r, t_m)$ can produce the time-domain images $\hat{x}_i(\tau, t_m)$ with further RFI suppression.

The entire block diagram of the proposed approach is shown in Figure 3. The left part of Figure 3 is the flowchart of the proposed suppression approach. The right part of Figure 3 is the schematic representation of the intermediate results at each processing step from Figure 2. The strong interferences in the magnitude image in the time domain of Figure 2(a) has been suppressed by channel equalization during imaging processing by NCSA. However, weak interferences are left with phase difference, as shown in Figure 3(a). Figures 3(b) and (c) give the detection results of magnitude and interferometric phase respectively, which are indicated by rectangles. By the median filtering in step 2, the magnitude of these weak interferences can be suppressed, as shown in Figure 3(d). The interferometric phase of image can be corrected by median filter in step 3, and the result is shown in Figure 3(e). All of figures in Figure 3 are in the frequency-time domain

with the vertical axis as cross-range slow time and the horizontal axis as range frequency.

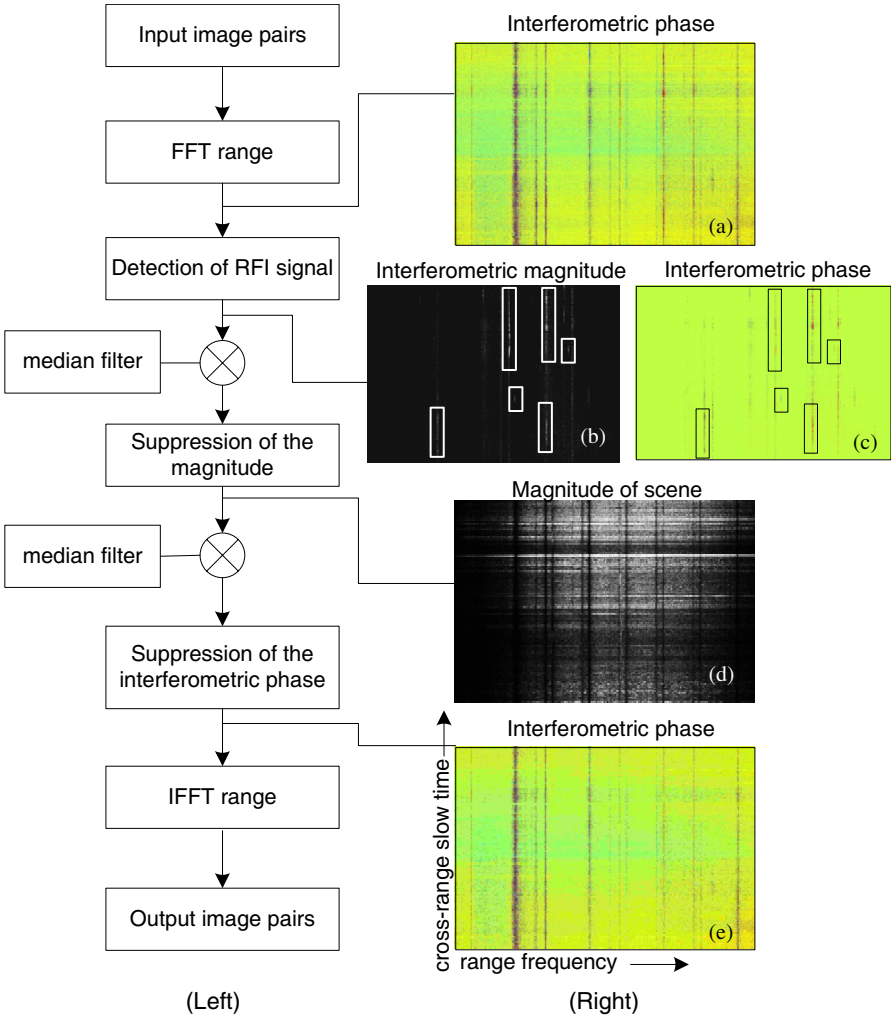

Figure 3. (Left) Block diagram of the proposed suppression approach. (Right) Schematic representation of the middle results at some processing steps.

4. THE COHERENCE IMPROVING ALGORITHM

In this part, we consider those mismatch errors that will reduce the coherence of the image pairs. The coherence ρ_γ between the complex image pair $x_i(\tau, t_m)$ after SAR imaging can be evaluated as:

$$\rho_\gamma = \frac{\left| \sum\limits_{\tau,t_m} \left[x_1(\tau,t_m)\, x_2^*(\tau,t_m) \right] \right|}{\sqrt{\sum\limits_{\tau,t_m} |x_1(\tau,t_m)|^2 \cdot \sum\limits_{\tau,t_m} |x_2(\tau,t_m)|^2}} \tag{20}$$

where $*$ denotes the complex conjugate operation, $\sum\limits_{\tau,t_m}$ is the sum of the pixels in the area to be evaluated [8, 27]. In low frequency system, the sources of these errors are mainly from frequency response of receiving channels, beam pattern and the motion of platform with the fluctuant ground clutter:

(a) The frequency response difference arises from the signal chain comprised of the radio frequency, baseband, sample-and-hold and A/D elements. We can calibrate the frequency mismatch errors from raw echo by equalizer in the 2-D frequency domain.

(b) The beam pattern difference arises from the differences of antenna in each channel. Since the antenna of each channel is installed independently on the platform, the beam pattern differences can be divided into two parts. One is the pointing deviation of the depression angle and the bearing cone angle [5–9], which may be caused by the installation error. The pointing deviation of the depression angle causes the mismatch of the range gate (i.e., the range fast time), while the pointing deviation of the bearing cone angle causes the mismatch of the Doppler frequency (i.e., the cross-range frequency). The beam pattern could vary from one pulse transmission to another because of heat and other uncontrollable natural factors that affect the internal circuitry. The other is the fixed error of antenna system itself [33–35], which will bring a constant error of magnitude and phase in the image pair This error can be corrected during the compensation of the registration error.

(c) The motion of platform like the attitude variations of aircraft and the atmospheric effects will distort the baseline in both along-track and vertical direction. The error between the designed along-track baseline and the real one causes the mismatch of images in slow time, while the vertical baseline error will cause the interferometric strip under the fluctuant ground clutter [36, 37]. This unwanted interferometric strip will also distort detection of the interferometric phase of moving target.

It is noted that the composition of the pointing deviation of the depression angle, the along-track baseline error and the fixed phase error of antenna system can be considered as the registration error of image pair. If the scene just contains static clutter and there is only the registration error in the image pair, the image of the second channel after compensation will be coincident with the image of the first channel. In this case, the image of the second channel can be expressed as:

$$x_2(\tau, t_m) = x_1(\tau + \Delta\tau, t_m + \Delta t_m) \exp(-j\phi_c) \tag{21}$$

where $\Delta\tau$ and Δt_m denote the shifts in the range fast time and the cross-range slow time, respectively, and ϕ_c the constant phase error of the image pair.

Low frequency SAR has wide beam angle, long synthetic aperture time, and the possible large bandwidth for high resolution imaging. The aforementioned errors have larger variation space than those in high frequency SAR. It is very important to correct these errors for coherence improving. It is noted that all mismatch errors can be compensated on the time domain or the frequency domain [8, 9]. The mismatch errors like the pointing deviation of the depression angle in the beam pattern can be compensated easily in the frequency domain. The correction of these errors can be expressed as:

$$X_2'(f_r, f_a) = X_2(f_r, f_a) G_f(f_r, f_a) \tag{22}$$

where $X_2'(f_r, f_a)$ denotes the image of the second channel after compensation in the frequency domain and $G_f(f_r, f_a)$ the errors to be compensated in the frequency domain. Theoretically, if there is only the error $G_f(f_r, f_a)$ in the image pair and the compensation is complete, $X_2'(f_r, f_a)$ will be equal to the image of the first channel in the frequency domain $X_1(f_r, f_a)$ in the pixels of static clutter. The mismatch errors from the extra vertical baseline and the fluctuant ground clutter can be compensated easily in the time domain. The correction of this error can be expressed as

$$x_2'(\tau, t_m) = x_2(\tau, t_m) g_t(\tau, t_m) \tag{23}$$

where $x_2'(\tau, t_m)$ denotes the image of the second channel after compensation in the time domain and $g_t(\tau, t_m)$ the errors to be compensated in the time domain. Since the low frequency SAR has a longer wavelength than the high frequency system, the local strip frequency of interferometric phase is lower than the one in high frequency system. Therefore, the variation of $g_t(\tau, t_m)$ is slow. Similarly, $x_2'(\tau, t_m)$ will be equal to the image of the first channel $x_1(\tau, t_m)$ in the pixels of static clutter, if there is only the error of $g_t(\tau, t_m)$.

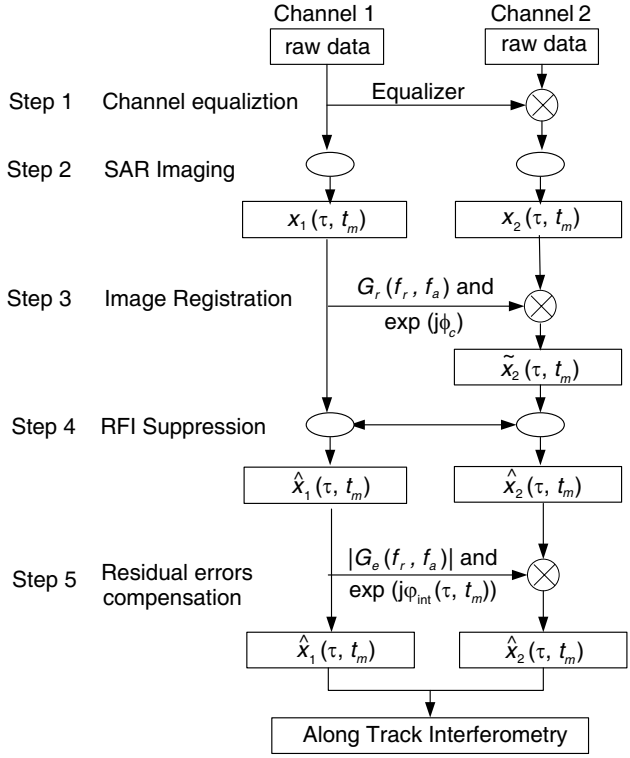

Figure 4. Block diagram of the proposed coherence improving algorithm.

Based on the contents in Section 3, we now propose the total pre-processing flow to improve coherence for the airborne along-track dual-channel low frequency SAR system The block diagram is shown in Figure 4 and the steps in details are as follows:

Step 1, channel equalization.

Select one channel as a reference channel, and calculate the equalizer in the closed loop before experiment sampling Then utilize the equalizer to compensate the frequency response difference of receiver channels by raw data. This step will reduce the sidelobe [28, 38] for the small time-bandwidth chirp signal at the same time [39].

Step 2, SAR imaging.

Complete SAR imaging of each channel, including the motion error compensation and the channel equalization for RFI suppression [21]. Channel equalization is an operational way in real data

processing. It can suppress those interferences with large energy and wide bandwidth, but it may leave weak and narrow bandwidth RFI unsuppressed. Different imaging algorithms may bring some signal processing errors. The same high precise imaging algorithm for both channels will reduce these errors [28–30]. The obtained image pair after imaging is $x_i(\tau, t_m)$.

Step 3 image registration.

Compensate the registration error of image pairs according to strong clutter in the SAR image. The mainlobes of strong static targets are hardly affected by unsuppressed RFI, especially when their magnitude are higher than -20 dB in the dB scaling SAR images. To avoid the heavy computation load, we can select the corresponding region of interest (ROI) in both channels, which contains the same strong targets. Then estimate the deviation of the maximum value in the 2-D frequency domain by interpolation, as well as the estimated mismatch errors $\Delta\tau$ and Δt_m. Both of them can be compensated in the frequency domain according to Equation (22), and $G_f(f_r, f_a)$ can be defined as

$$G_f(f_r, f_a) \triangleq G_r(f_r, f_a) = \exp(-j2\pi f_r \Delta\tau) \exp(-j2\pi f_a \Delta t_m) \quad (24)$$

The constant phase error ϕ_c can be estimated by the interferometric image of ROI in the time domain. To obtain a robust evaluation, the above estimation can be repeated in different ROIs. Finally, the registered image pair is obtained as $\tilde{x}_i(\tau, t_m)$.

Step 4 RFI suppression.

Use suppression algorithm in Section 3 to suppress RFI to satisfy the following detection of ATI. The renewed image pair is $\hat{x}_i(\tau, t_m)$.

Step 5 residual errors compensation.

The residual errors come from the beam pattern differences, the vertical baseline and other processing errors. This compensation includes two steps. First, select one channel as a reference channel and calibrate the magnitude differences $|G_e(f_r, f_a)|$ in the frequency domain by (22). Here $G_f(f_r, f_a) \triangleq |G_e(f_r, f_a)|$ The magnitude differences can be expressed as follows:

$$|G_e(f_r, f_a)| = \left| \hat{\widehat{X}}_1(f_r, f_a) / \hat{\widehat{X}}_2(f_r, f_a) \right| \quad (25)$$

where the 2-D images $\hat{\widehat{X}}_i(f_r, f_a)$ are transformed from the spectrum of ROI of strong static point targets by zeros padding. Second, use 2-D median filter to estimate the phase errors in the time domain

$$\varphi_{int}(\tau, t_m) = \text{MedFilter}[-\angle I(\tau, t_m)] \quad (26)$$

and compensate it on the interferometric image according to Equation (23), where $g_t(\tau, t_m) \triangleq \exp(j\varphi_{int}(\tau, t_m))$. Since this residual phase error mainly comes from the virtual vertical baseline, it varies slowly in the time domain. The multi-look image of the interferometric image $I(\tau, t_m)$ can be used in the median filtering. The filtering size should cover at least four times the number of pixels of moving targets. $I(\tau, t_m)$ is from the time domain image pair after the compensation of (25). Finally, we obtain the image pair $\widehat{x}_i(\tau, t_m)$ after this proposed algorithm.

This coherence improving algorithm synthesizes the main sources of errors in low frequency SAR. The median filtering used a lot in the novel approach is easy to implement in real-time processing. But this method only considers the slow variation of the magnitude and phase errors and the compensation only to the interferometric phase. It has little contribution to the clutter suppression.

5. SIMULATION AND EXPERIMENTAL RESULTS

In practice, the real velocities of uncooperative targets are unknown. It is also difficult to evaluate the accuracy of velocity estimation of the RFI suppression approach. Therefore, we first simulate scenes with RFI. These scenes contain static and moving targets with different magnitudes and radial velocities. The added RFI in the raw data lasts only 3 pulse repetition intervals with the magnitude of 6 dB comparing to a referenced static target, the bandwidth of 0.8 MHz and the phase difference $\Delta\varphi_l$ of 120°. Table 1 gives the mean and the standard deviation (STD) of the interferometric phase of each kind target under the cases without RFI, with RFI and after suppression using our approach. The results of each kind of target are concluded from the statistics of multiple targets at appointed magnitude and radial velocity. In this table, the weaker the energy of target is, the more serious influence the unsuppressed RFI has. After applying the proposed approach, the interferometric phases of both static clutter and moving targets approach to those without RFI. The velocity error can be expressed as:

$$\Delta v_r = \frac{\varepsilon}{2\pi}\frac{\lambda}{d}v_a \tag{27}$$

where d denotes the baseline of antenna phase center and λ the wavelength. $\varepsilon = \varepsilon_{|\Delta\bar{\phi}|} + \sigma_{\Delta\phi}$ is the sum of the mean error $\varepsilon_{|\Delta\bar{\phi}|}$ and the STD $\sigma_{\Delta\phi}$ (the square root of the variance). In Table 1, the bottom of the line gives a reference maximum value of $\varepsilon\left|\Delta\bar{\phi}\right| = 3.4°$ and $\sigma_{\Delta\phi} = 8.4°$. In this simulation, the parameter $\lambda v_a/d = 46$, thus

Table 1. The comparison of interferometric phase.

Interferometric phase		**mean $\Delta\bar{\phi}$ / STD$\sigma_{\Delta\phi}$ (degree)**		
		Without RFI	**With RFI**	**After suppression**
Static clutter	0 dB	0.01/0.22	−21.50/4.47	0.01/1.06
	−10 dB	0.05/0.41	−36.19/5.16	0.17/1.54
	−20 dB	0.13/0.99	−42.69/7.09	−0.59/3.18
Moving target	3 m/s, −10 dB	−23.49/2.54	−64.08/8.09	−19.24/2.72
	−3 m/s, −20 dB	23.30/2.59	39.77/5.65	17.43/3.31
	10 m/s, −10 dB	−78.47/6.57	−104.79/7.77	−76.99/6.00
	−10 m/s, −20 dB	78.06/7.69	17.46/8.27	84.50/8.31

the maximum estimation error for the radial velocity at 10 m/s has $\max(\Delta v_r) \approx 2$ m/s. If the baseline d is equal to the wavelength λ, there is an evaluation expression of the maximum velocity error $\max(\Delta v_r) = v_a \times 3.3\%$.

The total coherence improving algorithm has been tested on along-track interferometric P-band data, acquired by a NUDT's (National University of Defense Technology) experimental SAR system — the airborne strip-map dual-channel SAR. This system has a range bandwidth of 50 MHz with the centre slant range of 10 km. The velocity of the platform is within the range from 150 km/h to 300 km/h. The scene image via channel equalization and NCSA is given in Figure 2(a). In this scene, there is a broad runway along range time. Two cooperative vehicles with the same velocities are driving in sequence along this runway. Their positions are recorded by global position system (GPS). The area below the runway has lots of terraces. The area above the runway is near to the center of the city of Gui Yang in China, which has lots of interferences. Most of interferences have been suppressed by channel equalization during real-time processing. The magnitude image has satisfied the quality of its application. However, there are still weak and narrow band RFI signals left in the scene image as in Figure 2(b), which will distort the interferometric phase image.

Figure 5(a) shows an interferometric phase image, which is formed by the real-time image pair in Figure 2. Several strips in the range direction are clearly visible, caused by the RFI with phase differences of the image pair. Applying the proposed approach to both images, an improved interferometric phase image can be obtained, as shown

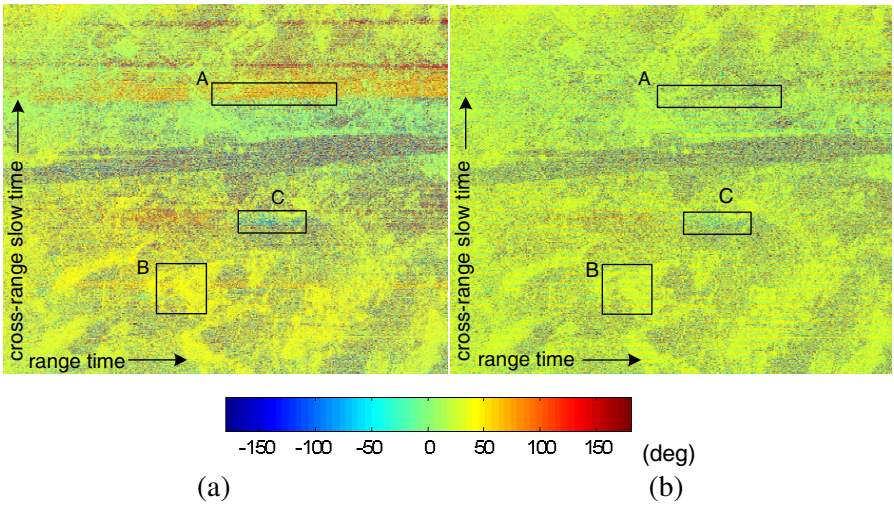

Figure 5. The interferometric phase image. (a) Formed by the real-time image pair with unsuppressed RFI. (b) After applying the proposed RFI suppression approach. The colorbar of interferometric phase is in the unit of degree.

Table 2. The proposed approach on the interferometric coherence.

Region in Figure 5	**A**	**B**	**C**
Before suppression	0.808	0.896	0.679
After suppression	0.928	0.981	0.797
After coherence improving	0.940	0.982	0.920

in Figure 5(b). Most of strips with obvious interferometric phase have disappeared. In Table 2, the coherences estimated for three regions in Figure 5 are given. Area-A represents an area which is significantly affected by RFI, area-B is almost unaffected, and area-C is an area which is affected by other unknown interferences. RFI is an important error source to interferometric phase; the original coherence is very low for interferometric image. If only using the proposed suppression approach, which has the same implementations to image pair, the coherence can be improved greatly by the proposed RFI suppression. However, there are still some room for further coherence improvement of the image pair in area-A and area-C because of other mismatch errors, as is shown in the bottom line of Table 2.

After using the total coherence improving algorithm, Figure 6 gives the final result of moving target detection by classical detection

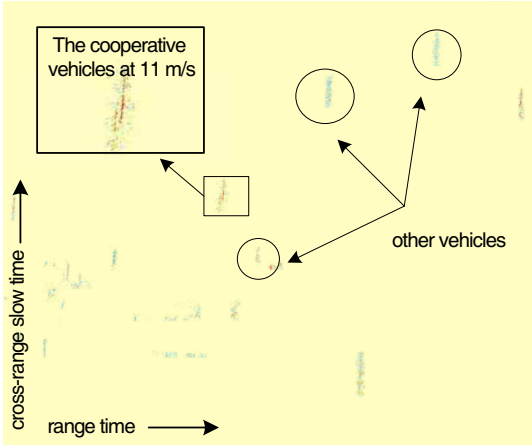

Figure 6. The final result of moving target detection based on the interferometric image of Figure 5(b). The colours of detected targets indicate the corresponding interferometric phase of radial velocity according to the colorbar in Figure 5.

method of ATI [1, 23, 27]. The two cooperative vehicles in large zoom are at the top left corner, whose velocities are consistent with the GPS recording. Some uncooperative vehicles are indicated by circles, which are clear after applying the approach.

Generally, this approach cannot be expected to revert the interferometric phase of moving targets perfectly. The interferences, with a phase difference of the image pair, may be left in the interferometric image, and they will affect the interferometric phase of moving target. However, when the weighting constant γ_0 and the threshold of interferometric phase $\Delta\bar{\vartheta}_m$ are chosen carefully, the influence from these interferences will be very small. It will not disturb moving target detection. The proposed pre-processing flow of coherence improving uses common median filters which has low computation load. This flow has a similar simple operation flow as moving target detection by ATI, so it is suitable for moving target detection in real-time.

6. CONCLUSION

In this paper, a novel pre-processing flow of coherence improving is proposed for GMTI in along-track dual-channel low frequency SAR, which considers RFI suppression for the along-track interferometric image. The novel RFI suppression approach is based on the focused

image in the range frequency and cross-range slow time domain. Analyses show that RFI signal in this domain is distributed as a line along the slow time, and can be easily detected in the interferometric image. The proposed approach can suppress weak interferences with the same implementations to the image pair. The total coherence improving pre-processing flow also focuses on the mismatch errors in along-track dual-channel low frequency SAR, including frequency response of receiving channels, beam pattern, and the motion of platform with the fluctuant ground clutter. This simple operation flow can be applied to real-time processing with low computation load. The experimental results highlight the effectiveness of the proposed algorithm and show that it is suitable in critical environments. The simulation results of suppression approach demonstrate the accuracy of this approach. The estimated error of radial velocity approaches to 3.3% of platform velocity when the baseline equals to the wavelength.

ACKNOWLEDGMENT

This research was supported in part by the Foundation for the Author of National Excellent Doctoral Dissertation of China under Grant 201046, in part by the Program for New Century Excellent Talents in University under Grants NCET-07-0223 and NCET-10-0895, and in part by the Hunan Provincial Innovation Foundation for Postgraduate under Grants CX2010B017.

REFERENCES

1. Tian, B., D. Y. Zhu, and Z. D. Zhu, "A novel moving target detection approach for dual-channel SAR system," *Progress In Electromagnetics Research*, Vol. 115, 191–206, 2011.
2. Chan, Y. K. and V. C. Koo, "An introduction to synthetic aperture radar (SAR)," *Progress In Electromagnetics Research B*, Vol. 2, 27–60, 2008.
3. Mao, X. H., D. Y. Zhu, L. Ding, and Z. D. Zhu, "Comparative study of RMA and PFA on their responses to moving target," *Progress In Electromagnetics Research*, Vol. 110, 103–124, 2010.
4. Chang, Y.-L., C.-Y. Chiang, and K.-S. Chen, "SAR image simulation with application to target recognition," *Progress In Electromagnetics Research*, Vol. 119, 35–57, 2011.
5. Ma, L., Z. F. Li, and G. S. Liao, "System error analysis and calibration methods for multi-channel SAR," *Progress In Electromagnetics Research*, Vol. 112, 309–327, 2011.

6. Xu, W. and Y. K. Deng, "Investigation on electronic azimuth beam steering in the spaceborne SAR imaging modes," *Journal of Electromagnetic Waves and Applications*, Vol. 25, Nos. 14–15, 2076–2088, 2011.
7. Umrani, A. W., "Effect of steering error vector and angular power distributions on beamforming and transmit diversity systems in correlated fading channel," *Progress In Electromagnetics Research*, Vol. 105, 383–402, 2010.
8. Wang, T., Z. Bao, Z. Zhang, and J. Ding, "Improving coherence of complex image pairs obtained by along-track bistatic SARs using range-azimuth prefiltering," *IEEE Transactions on Geoscience and Remote Sensing*, Vol. 46, No. 1, 3–13, 2008.
9. Lv, X., M. Xing, Z. Bao, S. Zhang, and Y. Wu, "Coherence improving algorithm for airborne multichannel SAR-GMTI," *IET Radar Sonar and Navigation*, Vol. 4, No. 3, 336–347, 2010.
10. Vu, V. T., T. K. Sjogren, M. I. Pettersson, H. J. Zepernick, and A. Gustavsson, "Experimental results on moving target detection by focusing in UWB low frequency SAR," *2007 IET International Conference on Radar Systems*, 1–5, 2007.
11. Yang, J., X. Huang, J. Thompson, T. Jin, and Z. Zhou, "Low frequency UWB SAR ground moving target imaging," *IET Radar, Sonar & Navigation*, Vol. 5, No. 9, 994–1001, 2011.
12. Du, Y., Y. L. Luo, W. Z. Yan, and J. A. Kong, "An electromagnetic scattering model for soybean canopy," *Progress In Electromagnetics Research*, Vol. 79, 209–223, 2008.
13. Chen, J., S. Quegan, and X. J. Yin, "Calibration of spaceborne linearly polarized low frequency SAR using polarimetric selective radar calibrators," *Progress In Electromagnetics Research*, Vol. 114, 89–111, 2011.
14. Miller, T., L. Potter, and J. McCorkle, "RFI suppression for ultra wideband radar," *IEEE Transactions on Aerospace and Electronic Systems*, Vol. 33, No. 4, 1142–1156, 1997.
15. Liu, Q., S. Xing, X. Wang, J. Dong, D. Dai, and Y. Li, "The interferometry phase of InSAR coherent jamming with arbitrary waveform modulation," *Progress In Electromagnetics Research*, Vol. 124, 101–118, 2012.
16. Liu, Q. F., S.-Q. Xing, X.-S. Wang, J. Dong, D.-H. Dai, and Y.-Z. Li, "The "SLOPE" effect of coherent transponder in InSAR DEM," *Progress In Electromagnetics Research*, Vol. 127, 351–370, 2012.
17. Potsis, A., A. Reigber, and K. P. Papathanassiou, "A phase

preserving method for RF interference suppression in P-band synthetic aperture radar interferometric data," *IEEE IGARSS'99*, 2655–2657, Hamburg, Germany, 1999.

18. Reigber, A. and L. Ferro-Famil, "Interference suppression in synthesized SAR images," *IEEE Geoscience and Remote Sensing Letters*, Vol. 2, No. 1, 45–49, 2005.
19. Vu, V. T., X. Sjögren, T. K. Gren, M. I. Pettersson, L. Håkansson, A. Gustavsson, and L. M. H. Ulander, "RFI suppression in ultrawideband SAR using an adaptive line enhancer," *IEEE Geoscience and Remote Sensing Letters*, Vol. 7, No. 4, 694–698, 2010.
20. Tian, J., Z. Zhimin, and S. Qian, "Subaperture wiener filter construction for time-varying RFI suppression in UWB SAR," *1st Asian and Pacific Conference on Synthetic Aperture Radar, 2007, APSAR 2007*, 71–75, Huangshan, China, 2007.
21. Dong, Z., D. Liang, and X. Huang, "A RFI suppression algorithm based on channel equalization for the VHF/UHF UWB SAR," *Journal Electronics & Information Technology*, Vol. 30, No. 3, 550–553, 2008.
22. Rosen, P. A., S. Hensley, and C. Le, "Observations and mitigation of RFI in ALOS PALSAR SAR data: Implications for the DESDYNI mission," *IEEE Radar Conference, 2008, Radar'08*, 1–6, Rome, Italy, 2008.
23. Gierull, C. H., "Digital channel balancing of along-track interferometric SAR data," *DRDC*, Canada, Ottawa, 2003.
24. Ren, S., W. Chang, T. Jin, and Z. Wang, "Automated sar reference image preparation for navigation," *Progress In Electromagnetics Research*, Vol. 121, 535–555, 2011.
25. Koo, V. C., Y. K. Chan, V. Gobi, M. Y. Chua, C. H. Lim, C.-S. Lim, C. C. Thum, T. S. Lim, Z. Bin Ahmad, K. A. Mahmood, M. H. Bin Shahid, C. Y. Ang, W. Q. Tan, P. N. Tan, K. S. Yee, W. G. Cheaw, H. S. Boey, A. L. Choo, and B. C. Sew, "A new unmanned aerial vehicle synthetic aperture radar for environmental monitoring," *Progress In Electromagnetics Research*, Vol. 122, 245–268, 2012.
26. Chua, M. Y. and V. C. Koo, "FPGA-based chirp generator for high resolution UAV SAR," *Progress In Electromagnetics Research*, Vol. 99, 71–88, 2009.
27. Gierull, C. H., "Statistical analysis of multilook SAR interferograms for CFAR detection of ground moving targets," *IEEE Transactions on Geoscience and Remote Sensing*, Vol. 42, No. 4, 691–701, 2004.

28. Cumming, I. G. and F. H. Wong, *Digital Processing of Synthetic Aperture Radar Data: Algorithms and Implementation*, Artech House Inc., Norwood, MA, USA, 2005.
29. An, D. X., Z.-M. Zhou, X.-T. Huang, and T. Jin, "A novel imaging approach for high resolution squinted spotlight SAR based on the deramping-based technique and azimuth NLCS principle," *Progress In Electromagnetics Research*, Vol. 123, 485–508, 2012.
30. Capozzoli, A., C. Curcio, and A. Liseno, "GPU-based ω-k tomographic processing by 1D non-uniform FFTs," *Progress In Electromagnetics Research M*, Vol. 23, 279–298, 2012.
31. Kay, S. M., *Modern Spectral Estimation: Theory and Application*, Prentice Hall, Englewood Cliffs, NJ, USA, 1988.
32. Fan, C. Y., X. T. Huang, Z. L. Xu, and T. Jin, "A RFI suppression approach based on along-track interferometric image," *2011 IEEE CIE International Conference on Radar*, Vol. 1, 214–218, Chengdu, China, 2011.
33. Sekretarov, S. and D. M. Vavriv, "A wideband slotted waveguide antenna array for SAR system," *Progress In Electromagnetics Research M*, Vol. 11, 165–176, 2010.
34. Habib, M. A., A. Bostani, A. Djaiz, M. Nedil, M. C. E. Yagoub, and T. A. Denidni, "Ultra wideband CPW-FED aperture antenna with WLAN band rejection," *Progress In Electromagnetics Research*, Vol. 106, 17–31, 2010.
35. Chen, A., T. Jiang, Z. Chen, and D. Su, "A novel low-profile wideband UHF antenna," *Progress In Electromagnetics Research*, Vol. 121, 75–88, 2011.
36. Li, S., H.-P. Xu, and L. Q. Zhang, "An advanced DSS-SAR InSAR terrain height estimation approach based on baseline decoupling," *Progress In Electromagnetics Research*, Vol. 119, 207–224, 2011.
37. Feng, L., H. P. Xu, C. S. Li, S. Li, and H. Gao, "A novel estimation approach of dynamic and coupling baseline for distributed satellite SAR," *Progress In Electromagnetics Research*, Vol. 123, 467–484, 2012.
38. Woo, J.-C., B.-G. Lim, and Y.-S. Kim, "Modification of the recursive sidelobe minimization technique for the range-Doppler algorithm of SAR imaging," *Journal of Electromagnetic Waves and Applications*, Vol. 25, No. 13, 1783–1794, 2011.
39. Lei, P. Z., H. Zhou, and X. T. Huang, "Multi-channel equalization for SAR/GMTI system with small time-bandwidth chirp signal," *2011 IEEE CIE International Conference on Radar*, Vol. 1, 707–710, Chengdu, China, 2011.